

28 **1. Introduction**

29 Terrestrial ecosystem evapotranspiration (E) is the primary pathway by which land surface
30 moisture returns to the atmosphere and thus plays a central role in the global water cycle (Liu et al.,
31 2023; Sun et al., 2022). E comprises three components: soil evaporation (Es), vegetation canopy
32 interception (Ei), and plant transpiration (T) (Niu et al., 2020; Wei et al., 2017). Among these,
33 vegetation transpiration, by which water is released to the atmosphere through plant stomata,
34 accounts for over 60% of total terrestrial E (Li et al., 2024; Wei et al., 2017). As transpiration is
35 closely linked to carbon assimilation and energy exchange, the vegetation transpiration fraction (TF,
36 defined as T/E) quantifies the contribution of vegetation to land–atmosphere water–vapor flux and
37 is a key indicator of vegetation–climate coupling strength (Schlesinger and Jasechko, 2014; Wei et
38 al., 2017). Understanding changes in TF is crucial for revealing ecohydrological mechanisms and
39 accurately predicting climate–change impacts.

40 Persistent climate warming and rising atmospheric CO₂ over the past few decades have driven
41 global vegetation greening and altered ecosystem water balances (Denissen et al., 2022; Hu et al.,
42 2023). Increases in Leaf area index (LAI) directly enhance canopy interception and transpiration
43 potential; global plant transpiration is estimated to have increased by about 6% from 1990–2020,
44 primarily as a consequence of increased LAI (Chen et al., 2024). However, the positive effect of
45 LAI on transpiration depends on water availability: when soil moisture (SM) is scarce or
46 atmospheric drought, often represented by vapor pressure deficit (VPD), intensifies, plants close
47 their stomata to suppress water loss, thereby reducing both transpiration and photosynthesis (Liu et
48 al., 2020b; Zahra et al., 2023). SM represents the supply-side constraint, whereas VPD represents
49 the atmospheric demand-side pull; these two factors often co-vary and can together impose
50 compound drought stress on ecosystems (Song et al., 2024). High VPD induces partial stomatal
51 closure to prevent excessive water loss and hydraulic failure, causing transpiration rates per unit
52 leaf area to saturate or even decline under very high VPD conditions (Grossiord et al., 2020; Novick
53 et al., 2016). Therefore, even as LAI increases, the additional leaf area struggles to further increase
54 T under extreme atmospheric drought (Xu et al., 2023). Conversely, under moderate SM and
55 appreciable atmospheric demand, vegetation can maintain both water supply and evaporative
56 demand at levels that support transpiration, allowing increases in LAI to exert a stronger positive

57 effect on TF (Liu et al., 2020a). During extreme soil drought, increased surface sensible heat further
58 dries the near-surface atmosphere, creating positive SM–VPD feedback that exacerbates drought
59 conditions (Qing et al., 2022; Zhou et al., 2019). Accurately characterizing the response of TF to
60 changes in LAI therefore requires a unified framework that accounts for the synergistic and
61 nonlinear effects of both soil water supply and atmospheric demand (Koehler et al., 2023). In recent
62 years, discrepancies have emerged regarding the relative roles of SM and VPD: some studies have
63 emphasized that atmospheric drought imposes greater limits on ecosystem water–carbon cycles
64 (Novick et al., 2016), whereas others, after decoupling the coupled effects of VPD and SM, have
65 found that soil moisture is the dominant factor, especially in semi-arid regions, where SM typically
66 imposes a stronger limitation on productivity (Liu et al., 2020a). Because SM and VPD are often
67 strongly correlated, quantifying their relative roles under coupled hydroclimatic conditions remains
68 a central challenge in ecohydrological research.

69 Since the 1970s, China has implemented some of the world’s largest-scale afforestation and
70 ecological restoration programs, increasing forest cover from approximately 12% in the 1970s to
71 over 22% in recent years (Cheng et al., 2025). China’s forests now comprise extensive natural and
72 planted forests. Natural forests are concentrated mainly in the mountainous regions of northeastern
73 and southwestern China, whereas planted forests are more widespread in eastern, central, and
74 southern China (Cheng et al., 2024b). Compared with natural forests, planted forests in China are
75 more often younger, structurally simpler, and dominated by single-species or even-aged stands
76 under more intensive management (Cheng et al., 2024a; Farooq et al., 2021). These differences in
77 origin, structure, and water-use strategies may underlie substantial disparities between NF and PF
78 in soil water acquisition, stomatal regulation, and hydraulic safety margins, thereby leading to
79 different responses of TF to changes in LAI (hereafter, LAI–TF sensitivity, denoted as θ). Exploring
80 these disparities between forest types can deepen the understanding of vegetation water-use
81 mechanisms and improve regional water-resource management, afforestation benefit assessment,
82 and climate-adaptive forestry strategies. However, systematic research on this issue is currently
83 lacking. Existing studies have mostly examined the sensitivity of transpiration or productivity to
84 drought stress at global or broad regional scales (Liu et al., 2020a; Novick et al., 2016) , or have
85 focused on ecohydrological processes in specific arid regions, without a comparative assessment of

86 θ across forest types along a unified climatic gradient. This raises four interrelated questions: (1)
87 Are there systematic differences in θ between NF and PF along the climatic gradient from humid to
88 semi-arid conditions? (2) How have these differences changed over the last 30 years? (3) Under
89 coupled changes in SM and VPD, what are the relative roles of these two factors in shaping θ , and
90 do these roles vary across climatic backgrounds or over time? (4) Through which hydrological
91 pathways (SM and/or VPD) do changes in macroclimate, such as radiation, precipitation,
92 temperature, and wind speed, indirectly affect θ ? Addressing these questions will help fill important
93 research gaps and deepen our understanding of forest–water relations under climate change.

94 The objectives of this study were to quantify the spatiotemporal patterns of transpiration
95 sensitivity (θ) in China’s natural forests (NF) and plantation forests (PF) from 1990 to 2020 and to
96 identify the hydroclimatic controls underlying these patterns. To this end, we integrated multi-
97 source remote-sensing and reanalysis data to derive growing-season LAI, evapotranspiration
98 components, and meteorological variables for forest pixels at 0.1° resolution. We first used the
99 aridity index (AI) framework to characterize the climatic background across four climatic zones and
100 then focused the statistical analyses on the humid, semi-humid, and semi-arid zones to ensure
101 comparability. We then applied complementary analytical approaches at different statistical scales:
102 pooled spatial binning was used to characterize the response surface of θ along the joint SM–VPD
103 gradient and to compare spatial contrasts under comparable hydroclimatic backgrounds, whereas
104 sliding-window partial correlation and ridge regression were used to quantify the independent
105 temporal associations of SM and VPD with θ and their evolution over time. Finally, pathway
106 analysis was used to decompose the indirect effects of macroclimate change on θ through local
107 hydrological pathways. All trends were estimated using the Theil–Sen slope and evaluated with the
108 Mann–Kendall test. We further assessed robustness through cross-product comparison and
109 examined whether atmospheric CO₂ and stand age altered the main interpretation. Together, this
110 framework was designed to reveal both the spatial heterogeneity and temporal evolution of
111 hydroclimatic controls on θ in China’s contrasting forest types.

112 **2. Materials and methods**

113 **2.1. Data**

114 We used datasets describing forest type, canopy structure, evapotranspiration components,

115 hydroclimate, and several auxiliary background factors (Table 1). Forest type data were obtained
116 from the 1990–2020 spatial distribution dataset of natural and plantation forests in China (Cheng et
117 al., 2024b). This dataset was derived from Landsat imagery and extensive forest inventory samples
118 using machine-learning classification and was resampled to 0.1° resolution to match the
119 hydroclimatic datasets. Pixels with 100% coverage of either natural forest (NF) or plantation forest
120 (PF) were treated as pure pixels, and only these pixels were included in all major analyses. To
121 maintain temporal consistency between forest masks and climate data, we adopted a period-based
122 dynamic matching strategy. Specifically, forest maps for 1990, 1995, 2000, 2005, 2010, 2015, and
123 2020 were used to represent the periods 1990–1994, 1995–1999, 2000–2004, 2005–2009, 2010–
124 2014, 2015–2019, and 2020, respectively.

125 LAI was derived from the GIMMS LAI4g dataset (Cao et al., 2023). The main
126 evapotranspiration dataset used in this study was GLEAM v4.2a, from which transpiration (T),
127 evapotranspiration (E), and soil moisture (SM) were extracted. GLEAM separately estimates the
128 major components of terrestrial evaporation and provides both surface and root-zone soil moisture.
129 In this study, SM refers to the root-zone soil moisture product, rather than surface soil moisture,
130 because it more closely represents plant-available water relevant to transpiration regulation at the
131 seasonal to interannual scales considered here. In GLEAM, root-zone soil moisture is represented
132 as a vegetation-accessible multi-layer soil profile constrained by assimilated surface observations,
133 rather than as a single shallow soil layer. Near-surface meteorological variables, including air
134 pressure (Pa), relative humidity (RH), air temperature (Ta), precipitation (P), dewpoint temperature
135 (Td), wind speed (WS), net radiation (Rn), and potential evapotranspiration (PET), were obtained
136 from ERA5-Land. All environmental variables were aggregated over the growing season (April–
137 October) for 1990–2020, using only growing-season data and excluding non-growing-season
138 observations. Means were used for state variables (e.g., LAI, SM, Ta, and VPD), whereas
139 cumulative values were used for flux variables (e.g., E, T, and P).

140 To evaluate the robustness of the estimated θ patterns and trends to data-product choice, we
141 additionally used two alternative gridded products for cross-product comparison in supplementary
142 analyses. One was the Simple Terrestrial Hydrosphere v2 (SiTHv2) product, which provides
143 independent estimates of evapotranspiration and transpiration (Zhang et al., 2024). The other was

144 the China terrestrial ecosystem transpiration fraction dataset (Niu et al., 2020), from which an
 145 alternative transpiration-fraction-based θ estimate was derived for comparison. These two datasets
 146 were used only for robustness assessment of θ , whereas all main calculations in the study were based
 147 on GLEAM.

148 To assess whether long-term changes in θ may also be modulated by non-hydroclimatic
 149 background factors, we further compiled several auxiliary datasets for supplementary analyses,
 150 including a global 1-km atmospheric carbon dioxide concentration dataset (Wang, 2026), a long-
 151 term reconstructed forest age dataset for China (Xia et al., 2023), and a 2020 forest age spatial
 152 distribution dataset for China (Cheng et al., 2024a). These auxiliary datasets were resampled to 0.1°
 153 resolution and used only to assess whether CO_2 and stand age materially altered the observed θ
 154 patterns and trends. They were not included in the main analytical framework, in which the focus
 155 was on hydroclimatic controls.

156 **Table 1. Data overview**

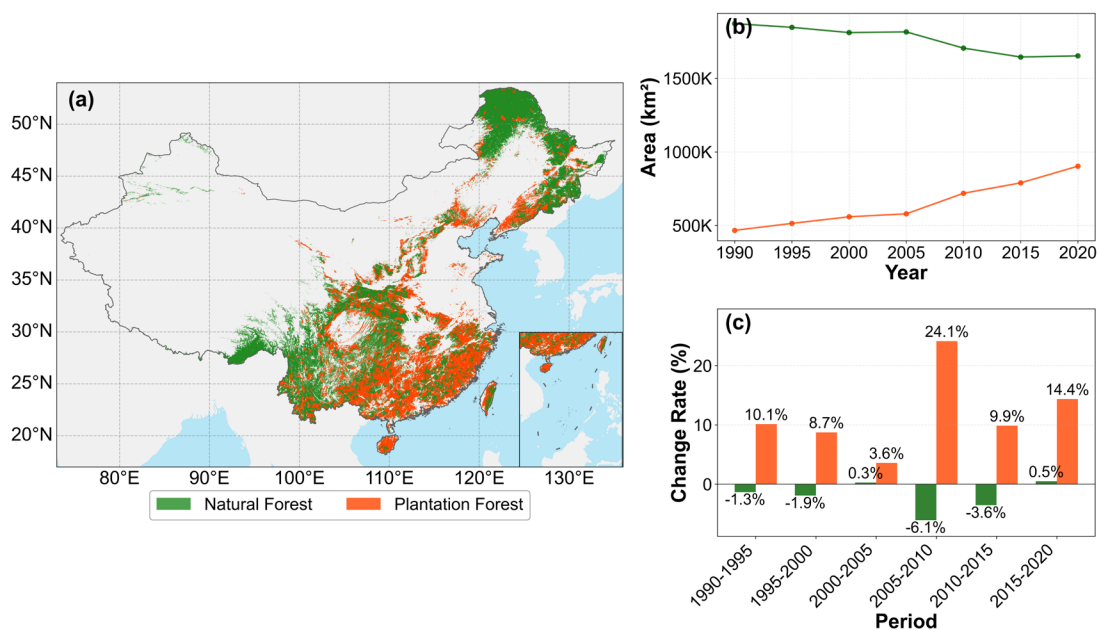
Variable	Data set	Resolution (spatial)	Resolution (temporal)	Time span	References
Forest type	Planted and natural forest maps in China from 1990 to 2020	1 km	5 years	1990– 2020	Cheng et al., 2024b
LAI	GIMMS LAI4g	$1/12^\circ$	15 day	1982– 2020	Cao et al., 2023
E, T, SM	GLEAM v4.2a	0.1°	1 day	1980– 2023	Miralles et al., 2025
Validation data	SiTHv2	0.1°	1 day	1982– 2020	Zhang et al., 2024
	China terrestrial ecosystem transpiration fraction dataset	0.05°	8 day	1981– 2015	Niu et al., 2020
Ta, Pa, RH, Td, P, PET, Rn, WS	ERA5-Land	0.1°	1 month	1950– 2025	Muñoz-Sabater et al., 2021
CO ₂	Global 1 km atmospheric carbon dioxide concentration dataset	1 km	annually	2003– 2023	Wang, 2026
forest age	Long-term reconstructed forest age dataset for China	1 km	annually	1980– 2015	Xia et al., 2023
	2020 forest age spatial distribution dataset for China	30 m	static	2020	Cheng et al., 2024a

157 LAI, Leaf area index; E, Evapotranspiration; T, Transpiration; SM, Root-zone soil moisture; Ta,

158 Air temperature; Td, Dewpoint temperature; Pa, Air pressure; P, Precipitation; PET, Potential
 159 evapotranspiration; Rn, Net radiation; WS, wind speed.

160 2.2. Study region

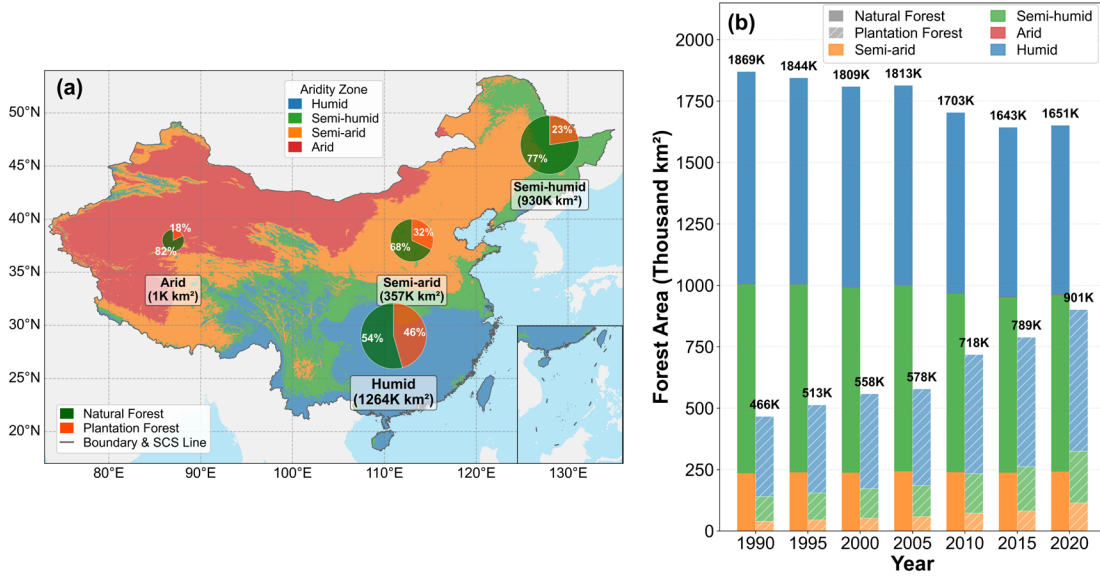
161 Our study area covers terrestrial China, spanning temperate, subtropical, and tropical climate
 162 zones. The analysis focuses on China's NF and PF. NF are mainly concentrated in the mountains of
 163 Northeast and Southwest China, whereas PF are widely distributed across the plains and hills of
 164 East, Central, and South China (Figure 1a). The vast majority of NF and PF are located in humid
 165 and semi-humid zones (Figure 2).



166
 167 **Figure 1. Spatiotemporal characteristics of China's natural forests (NF) and plantation forests**
 168 **(PF) from 1990 to 2020.** (a) Average spatial distribution of NF (green) and PF (orange) in China
 169 from 1990 to 2020. (b) Dynamic changes in the area (km²) of NF and PF from 1990 to 2020. (c)
 170 Rate of change (%) in NF and PF area for each five-year period from 1990–2020.

171 We used the aridity index (AI) to characterize climatic background and to organize the spatial
 172 analyses within a unified framework. AI was defined as the ratio of annual potential
 173 evapotranspiration to annual precipitation ($AI = PET / P$). Based on the 1990–2020 multi-year mean
 174 AI, China was divided into four climatic zones: humid ($AI < 1$), semi-humid ($1 \leq AI < 1.5$), semi-
 175 arid ($1.5 \leq AI < 4$), and arid ($AI \geq 4$). This four-zone classification was used as the geographic
 176 framework for mapping and descriptive comparisons. Because forest samples in the arid zone were

177 extremely sparse, subsequent statistical analyses were restricted to the humid, semi-humid, and
 178 semi-arid zones.



179
 180 **Figure 2. Spatiotemporal distribution and composition of forests in different climatic zones in**
 181 **China from 1990 to 2020.** (a) Spatial distribution of the four climatic zones (humid, semi-humid,
 182 semi-arid, and arid) in China; the pie charts show the total forest area within each zone and its
 183 composition of natural forest (green) and planted forest (orange). (b) Dynamic changes in forest
 184 area in each climatic zone from 1990 to 2020. For each year, the left solid stacked bar represents
 185 natural forest (NF), and the right hatched stacked bar represents plantation forest (PF). Bar colors
 186 indicate the forest area contributed by different climatic zones. The value at the top of each year
 187 indicates the total national forest area, and labels with “K” denote 10³ km².

188 2.3. Methods

189 2.3.1. VPD calculation

190 Vapor pressure deficit (VPD, hPa) is expressed, as follows, as the difference between
 191 saturation vapor pressure (P_s , hPa) and actual vapor pressure (P_w , hPa):

$$192 \quad VPD = P_s - P_w \quad (1)$$

193 To calculate VPD, we used directly observed meteorological parameters, including air
 194 temperature (T_a , °C), relative humidity (RH , %), and air pressure (P_a , hPa). P_s was calculated using
 195 the improved Magnus equation (Yuan et al., 2019):

$$196 \quad P_s = 6.112 \times f \times e^{\frac{17.67 \times T_a}{T_a + 243.5}} \quad (2)$$

197 Here, f is the atmospheric pressure enhancement factor, which corrects for the effect of pressure
 198 on saturation vapor pressure in moist air (Buck, 1981). This coefficient is calculated using P_a as
 199 follows:

$$200 \quad f = 1 + 7 \times 10^{-4} + 3.46 \times 10^{-6} \times P_a \quad (3)$$

201 P_w is then derived from P_s and RH as follows :

$$202 \quad P_w = P_s \times RH \times \frac{1}{100\%} \quad (4)$$

203 **2.3.2. Sensitivity of TF to LAI**

204 We define the transpiration fraction as

$$205 \quad TF = \frac{T}{E} \quad (5)$$

206 In this study, T and E were first aggregated from daily data to annual growing-season totals
 207 (April–October), and LAI was represented by the corresponding annual growing-season mean. TF
 208 was then calculated from these annual growing-season quantities, and all subsequent θ analyses
 209 were therefore conducted at the annual growing-season scale rather than at the daily or monthly
 210 scale.

211 Note that $TF \in (0,1)$ is bounded. To explicitly account for the inherent nonlinearity and
 212 saturation in the TF–LAI relationship, we estimated the sensitivity θ as a marginal response under
 213 a bounded nonlinear framework.

214 Within the full period (1990–2020) and within each 11-year moving window, we fit a quadratic
 215 model in logit space:

$$216 \quad z = \text{logit}(TF) = \ln\left(\frac{TF}{1-TF}\right) = a + b(LAI - LAI_{med}) + c(LAI - LAI_{med})^2 \quad (6)$$

217 Here, LAI_{med} is the pixel-specific median LAI within the same period (median-centering was
 218 used to improve numerical stability). Prior to the logit transform, TF was clipped to $[\varepsilon, 1 - \varepsilon]$ ($\varepsilon =$
 219 0.005) to avoid numerical singularities.

220 We then recovered $\widehat{TF} = 1 / (1 + e^{-z})$ and computed the marginal sensitivity as

$$221 \quad \theta = \frac{\partial TF}{\partial LAI} = \widehat{TF} (1 - \widehat{TF}) [b + 2c(LAI - LAI_{med})] \quad (7)$$

222 For ease of interpretation, Eq. (7) can be written as

223 $\theta = \underbrace{\widehat{TF}(1-\widehat{TF})}_{damping} \times \underbrace{[b + 2c(LAI - LAI_{med})]}_{\eta}$, in which the damping term reflects boundary effects

224 and η represents the structural sensitivity in logit space.

225 To separate the position-dependent saturation effect from changes in the shape of the fitted TF-
 226 LAI relationship, we evaluated (i) θ_{total} at $LAI = LAI_{med}$, representing the sensitivity under the
 227 actual state of each pixel and (ii) θ_{clim} at a fixed reference LAI_{ref} (global median LAI), which
 228 removes the influence of shifting along the TF-LAI curve. Additionally, the boundary component
 229 was quantified as

$$230 \quad \theta_{bound} = \theta_{total} - \theta_{clim} \quad (8)$$

231 We calculated θ at two time scales. (1) The full-period mean θ characterized the average state
 232 during 1990–2020. (2) The θ time series characterized decadal changes, generated using an 11-year
 233 moving window recorded for the central year (1995–2015), a data processing step that was also used
 234 for subsequent trend and attribution analyses. Pixels with insufficient valid years and negligible LAI
 235 variability were excluded to ensure robustness.

236 We further used a fixed-curve counterfactual decomposition to separate the temporal change
 237 in θ_{total} into a position/saturation effect and a shape effect. The position effect describes changes in
 238 θ caused by LAI moving along an otherwise fixed TF-LAI curve, and therefore reflects the bounded
 239 nature of TF and the saturation compression associated with $TF(1-TF)$. In contrast, the shape effect
 240 describes changes in θ caused by temporal changes in the fitted TF-LAI curve itself, as reflected by
 241 changes in the logit-quadratic coefficients.

242 For each forest type, the first 11-year window was used as the reference curve. The fixed-curve
 243 prediction was calculated by holding the regression coefficients of this reference curve constant
 244 while allowing LAI to vary through time. The position effect was then defined as the change
 245 predicted by this fixed-curve model, whereas the shape effect was defined as the residual between
 246 the observed θ_{total} trajectory and the fixed-curve prediction. Thus,

$$247 \quad \Delta\theta_{total} = \Delta\theta_{position} + \Delta\theta_{shape} \quad (9)$$

248 Where $\Delta\theta_{position}$ represents movement along a fixed bounded response curve and $\Delta\theta_{shape}$
 249 represents changes in the response-curve shape.

250 **2.3.3. Spatial association under the joint SM–VPD gradient: binning analysis**

251 To assess the relative roles of SM and VPD in the spatial differentiation of θ , we applied a
252 pooled spatial-binning analysis. Using all eligible pure NF and pure PF pixels as samples, we
253 extracted the full-period mean θ , SM, and VPD values and Z-score standardized them. To evaluate
254 the relative effect of VPD under comparable SM backgrounds, denoted as $\Delta\theta(\text{VPD}|\text{SM})$, pixels
255 were first grouped into bins according to SM. Within each SM bin, the difference in mean θ between
256 high- and low-VPD groups was calculated, and these differences were then averaged across bins.
257 The relative effect of SM, denoted as $\Delta\theta(\text{SM}|\text{VPD})$, was evaluated in the same way by binning
258 pixels according to VPD and then comparing high- and low-SM groups within each bin. This
259 approach thus summarized spatial contrasts under comparable hydroclimatic backgrounds using a
260 control-variable logic. These analyses are complementary but not identical to the subsequent
261 temporal attribution analyses; specifically, the binning analysis characterized cross-site contrasts in
262 θ across the long-term SM–VPD climate space, whereas the partial-correlation and ridge analyses
263 quantified within-pixel temporal associations of θ with SM and VPD.

264 **2.3.4. Dynamic temporal attribution: partial correlation and ridge regression**

265 To investigate the pixel-scale temporal relationships of SM and VPD with θ , we used partial
266 correlation and ridge regression based on the 1995–2015 11-year sliding-window series. This
267 analysis was conducted at two levels. First, for each pixel, we calculated an overall partial
268 correlation coefficient and ridge-regression coefficient based on the full 1995–2015 series,
269 representing the average independent association of SM and VPD with θ throughout that period
270 after accounting for their covariation. Second, to evaluate change over time, we performed a
271 secondary sliding-window analysis on the same 1995–2015 series and generated time series of the
272 coefficients themselves. Trends in these coefficient series were then used to infer whether the effects
273 of SM and VPD became stronger or weaker over time. Thus, the first-level analysis described the
274 mean temporal attribution pattern, whereas the second-level analysis characterized its change over
275 time.

276 Partial correlation analysis: We calculated two pixel-wise partial correlation coefficients: $r(\theta,$
277 $\text{SM}|\text{VPD})$ and $r(\theta, \text{VPD}|\text{SM})$. The former represents the correlation between θ and SM after
278 controlling for interannual VPD fluctuations, whereas the latter represents the correlation between

279 θ and VPD after controlling for SM variability.

280 Ridge regression analysis: Given the collinearity between SM and VPD, we further employed
281 a ridge regression model, $\theta = \beta_{SM} \cdot SM + \beta_{VPD} \cdot VPD$, to more robustly quantify their relative
282 contributions to θ . By introducing an L2 regularization term, ridge regression stabilizes coefficient
283 estimates under multicollinearity. The regression was performed on standardized time series, and
284 the resulting coefficients (β_{SM} and β_{VPD}) directly reflect the relative strengths of the SM and VPD
285 effects. We further calculated the relative contribution (RC) of SM and VPD as
286 $RC_{SM} = |\beta_{SM}| / (|\beta_{SM}| + |\beta_{VPD}|)$ and $RC_{VPD} = |\beta_{VPD}| / (|\beta_{SM}| + |\beta_{VPD}|)$, to determine the
287 dominant hydrological driver at each pixel. To further diagnose multicollinearity between SM and
288 VPD, we also calculated the variance inflation factor (VIF).

289 To quantify temporal changes in θ and in the coefficient series derived from the 11-year
290 moving-window analysis, we estimated trends using the Theil–Sen median slope estimator. Trend
291 significance was assessed using the Mann–Kendall (MK) test (two-tailed, $\alpha = 0.05$). To reduce
292 potential bias caused by temporal autocorrelation, the MK statistic was variance-corrected. The
293 same trend-analysis framework was applied consistently to all moving-window-derived time series
294 used in the temporal attribution analysis.

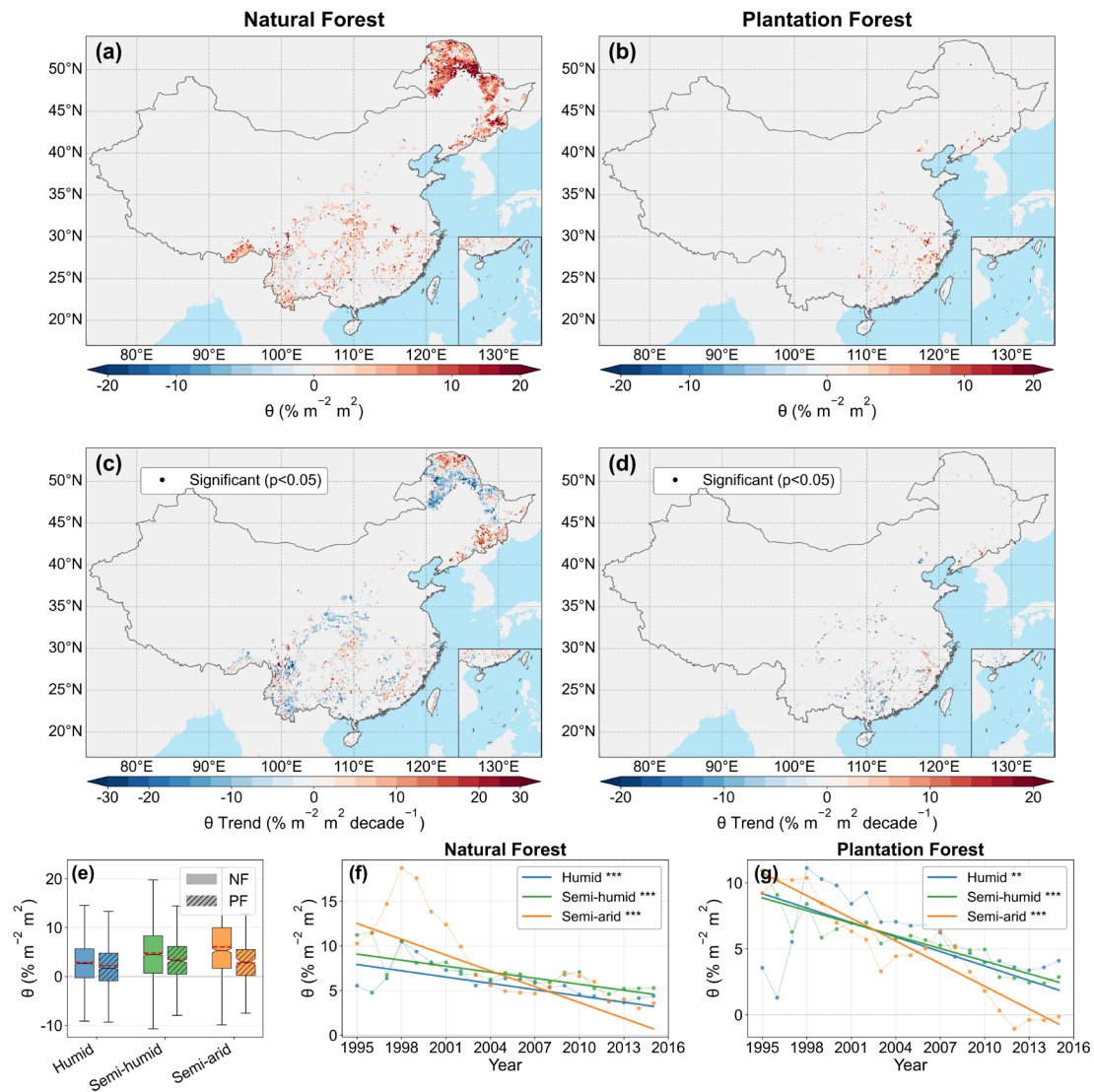
295 **2.3.5. Pathway analysis of macroclimate effects on θ**

296 To analyze the pathways through which macroclimate change may affect θ via local
297 hydrological processes, we constructed a pathway model. The independent variable X served as the
298 climate-factor trend (including P, Ta, Rn, and WS), the mediator variable M corresponded to the
299 local water supply–demand status (SM and VPD trends), and the dependent variable Y represented
300 the θ trend. RH was not included separately because its effect on atmospheric water demand is
301 already represented by VPD. Pathway analysis was used to partition the associations between
302 macroclimate trends and θ into direct effects and indirect effects mediated through SM and VPD.
303 The statistical significance of all pathway effects was tested by bootstrap resampling (1000
304 iterations). Because SM and VPD may remain correlated under coupled hydroclimatic conditions,
305 the pathway coefficients were interpreted as complementary association pathways rather than as a
306 strict causal separation of two fully independent mediators. This interpretation was further evaluated

307 using a supplementary mediator-specification comparison based on SM-only, VPD-only, and joint
 308 pathway models (Figure S19). The trends of P, Ta, Rn, WS, SM, VPD, and θ used in the pathway
 309 analysis were all estimated using the same Theil–Sen and variance-corrected Mann–Kendall
 310 framework described above.

311 3. Results

312 3.1. Spatiotemporal patterns and long-term trends of θ

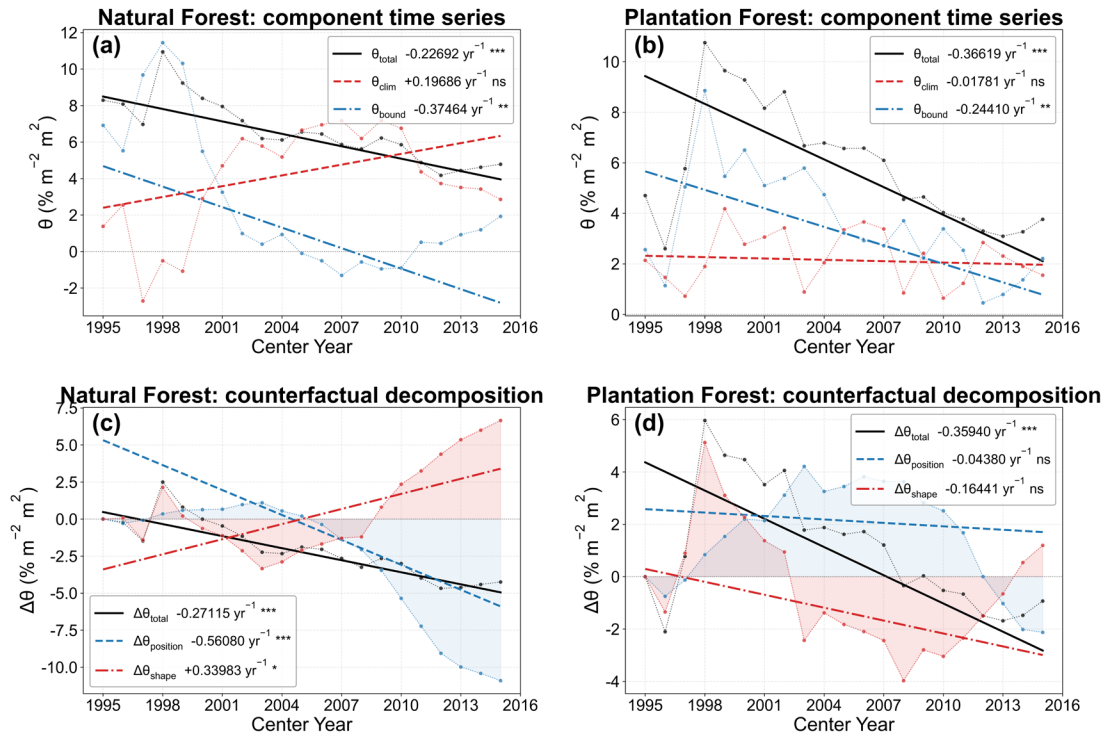


313
 314 **Figure 3. Spatiotemporal patterns and long-term trends of LAI—TF sensitivity (θ) in China's**
 315 **natural forests (NF) and plantation forests (PF) during the 1990–2020 growing seasons. (a)**
 316 **and (b) show the multi-year mean spatial distribution of θ for NF and PF, respectively, derived from**
 317 **the overall logit–quadratic model using TF_E . (c) and (d) show the corresponding long-term trends**
 318 **in θ estimated from the 11-year moving-window time series using the Theil–Sen slope; black dots**

319 indicate significant trends based on the Mann–Kendall test ($p < 0.05$). (e) shows the distribution of
320 θ across climatic zones (humid, semi-humid, and semi-arid) for NF and PF. (f) and (g) show the
321 temporal evolution of zone-averaged θ for NF and PF, respectively, with Theil–Sen trend lines
322 overlaid.

323 Mean θ showed clear spatial heterogeneity and was consistently higher in NF than in PF
324 (Figure 3a, b, e). High- θ areas in NF were concentrated mainly within the semi-arid to semi-humid
325 transition belt, whereas PF showed a distinctly more fragmented pattern. During 1990–2020,
326 growing-season θ declined widely in both forest types, with a stronger mean decline in PF than in
327 NF (Figure 3c, d). Significant negative trends were concentrated mainly in semi-humid and semi-
328 arid transition regions, while humid regions showed weaker negative trends. The zone-averaged
329 time series further confirmed that θ decreased significantly across climatic zones in both forest types,
330 with the strongest declines occurring under drier climatic conditions (Figure 3f, g). Overall, the
331 marginal enhancement of TF by increasing LAI weakened over the past three decades, especially in
332 PF and in relatively dry regions.

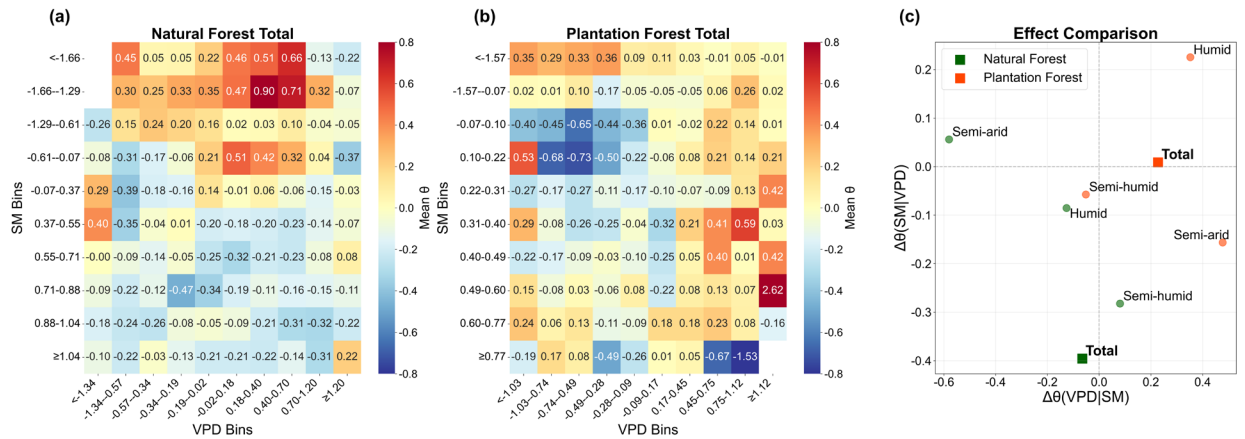
333 The decomposition of θ_{total} provided additional insight into the mechanisms behind the
334 observed decline (Figure 4). Under the main TFE definition, the long-term decrease in θ_{total} reflected
335 both position-dependent saturation and changes in the fitted TF–LAI curve shape, but their relative
336 roles differed between forest types. In natural forests, the position/saturation component made a
337 negative contribution to θ_{total} , whereas the shape component differed in sign and partly offset the
338 decline. This contrast indicates that the total θ trend would be difficult to interpret from θ_{total} alone.
339 In plantation forests, the position/saturation component also contributed to the weakening of θ_{total} ,
340 while the shape component indicated additional changes in the fitted TF–LAI sensitivity. These
341 results show that the weakening of the LAI enhancement effect on TF is not merely a bounded
342 geometric consequence of higher LAI or TF approaching saturation; it also reflects changes in the
343 biophysical TF–LAI relationship under evolving hydroclimatic conditions.



344

345 **Figure 4. Decomposition of temporal changes in LAI–TF sensitivity (θ) into**
 346 **position/saturation and shape/climate-related components. (a, b) Time series of spatially**
 347 **averaged θ_{total} , θ_{clim} , and θ_{bound} for natural forests (NF) and plantation forests (PF), respectively,**
 348 **under the main TFE definition. (c, d) Counterfactual decomposition of $\Delta\theta_{\text{total}}$ into $\Delta\theta_{\text{position}}$ and**
 349 **$\Delta\theta_{\text{shape}}$ for NF and PF, respectively. The fixed-curve null model holds the logit-quadratic regression**
 350 **coefficients at their first-window values while allowing LAI to vary, so $\Delta\theta_{\text{position}}$ reflects movement**
 351 **along a fixed bounded TF–LAI curve. $\Delta\theta_{\text{shape}}$ is the residual between the observed trajectory and the**
 352 **fixed-curve prediction and reflects changes in the fitted response-curve shape. Lines indicate Theil–**
 353 **Sen trends; significance was evaluated using the Mann–Kendall test.**

354 **3.2. Hydroclimatic controls of θ : SM and VPD**
 355 **3.2.1. Response of θ to the joint SM–VPD gradient**



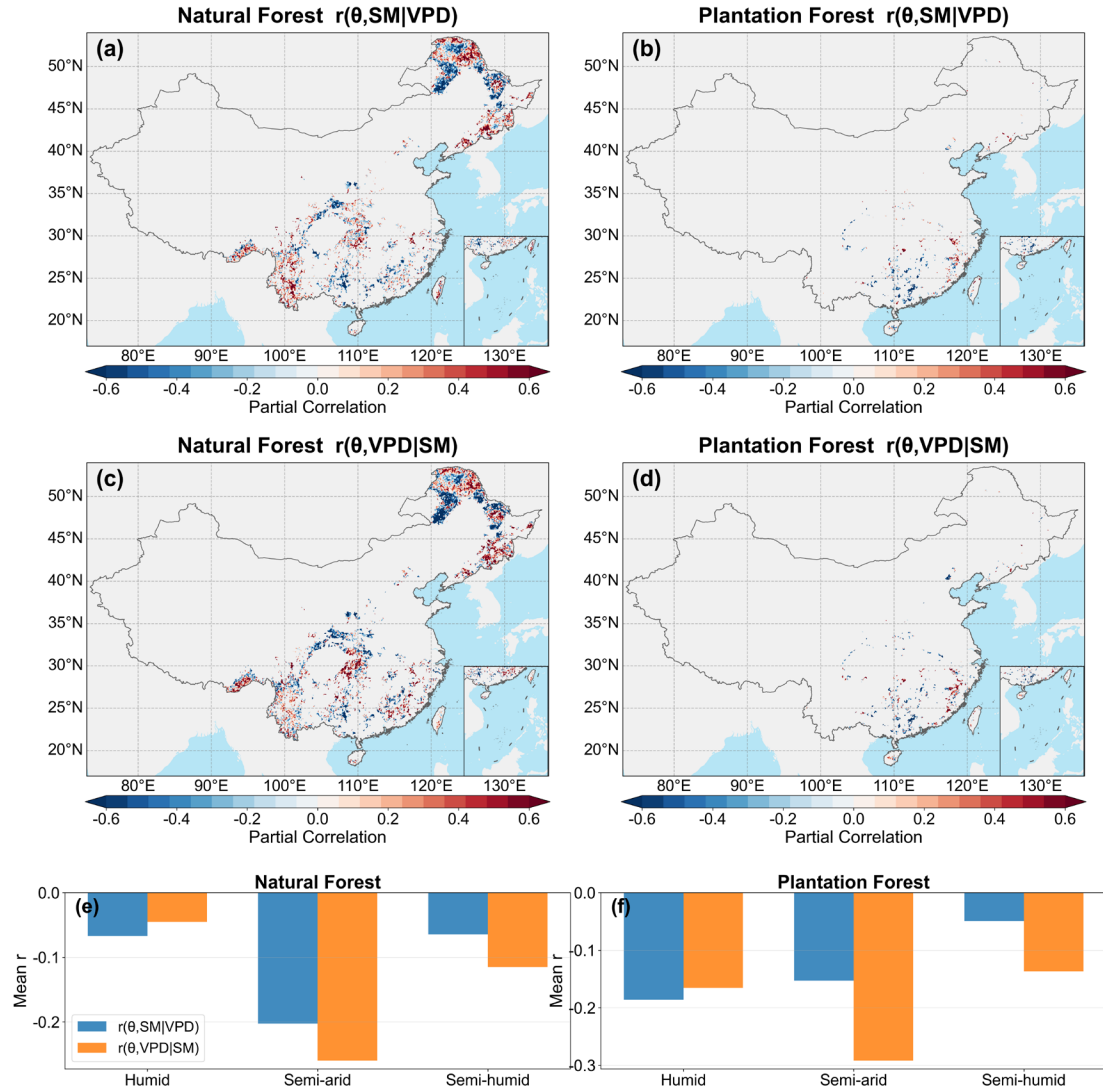
356
 357 **Figure 5. Pooled spatial binning analysis of LAI–TF sensitivity (θ) under the joint soil**
 358 **moisture (SM)–vapor pressure deficit (VPD) gradient during the 1990–2020 growing seasons.**
 359 (a) and (b) show the mean standardized θ values in 10×10 SM–VPD bins for natural forests (NF)
 360 and plantation forests (PF), respectively; only bins with sample size ≥ 10 are shown. (c) shows the
 361 relative effects of VPD and SM as indicated by $\Delta\theta(\text{VPD}|\text{SM})$ and $\Delta\theta(\text{SM}|\text{VPD})$, calculated from
 362 the top 20% versus bottom 20% contrasts within each bin and then averaged across bins. Circles
 363 denote climatic zones, while squares denote the national total. θ was Z-score standardized in this
 364 analysis.

365 Pooled binning analysis showed that θ varied nonlinearly along the joint SM–VPD gradient in
 366 both forest types, with relatively high values occurring under intermediate SM and moderate-to-
 367 high VPD conditions, and lower values toward both the wet/low-VPD and dry/high-VPD ends of
 368 the gradient (Figure 5a,b). The contrast analysis further revealed clear differences in the relative
 369 effects of SM and VPD (Figure 5c). At the national scale, NF showed a much stronger SM-related
 370 contrast than VPD-related contrast [$\Delta\theta(\text{SM}|\text{VPD}) = -0.396$ versus $\Delta\theta(\text{VPD}|\text{SM}) = -0.065$], whereas
 371 PF showed the opposite pattern, with a much stronger VPD-related contrast [$\Delta\theta(\text{VPD}|\text{SM}) = 0.228$
 372 versus $\Delta\theta(\text{SM}|\text{VPD}) = 0.009$]. Across climatic zones, NF exhibited stronger VPD-related contrasts
 373 in the humid and semi-arid zones but stronger SM-related contrasts in the semi-humid zone. In
 374 contrast, PF was mainly VPD-dominated in the humid and semi-arid zones, while both contrasts
 375 were relatively weak in the semi-humid zone. Within the pooled spatial-binning framework, these
 376 results indicate that the relative roles of soil water supply and atmospheric demand differed

377 markedly between NF and PF. Zone-specific pooled SM–VPD binning patterns for NF and PF are
378 shown in Figures S14 and S15, respectively.

379 **3.2.2. Dynamic evolution of the independent effects of SM and VPD**

380 Partial-correlation analysis revealed that the independent associations of θ with both SM and
381 VPD were predominantly negative and were generally stronger in PF than in NF (Figure 6). At the
382 national scale, the mean values of $r(\theta, \text{SM}|\text{VPD})$ and $r(\theta, \text{VPD}|\text{SM})$ were -0.0725 and -0.0992 in
383 NF, compared with -0.1517 and -0.1630 in PF, respectively, indicating slightly stronger VPD-
384 related associations in both forest types and overall stronger hydroclimatic constraints in PF. Across
385 climatic zones, the strongest negative partial correlations in NF occurred in the semi-arid zone,
386 especially for VPD, whereas PF showed consistently negative correlations across all zones. The
387 temporal analyses further revealed spatially heterogeneous changes in these relationships (Figure
388 7). In NF, the SM-related partial correlation became less negative in the humid and semi-arid zones,
389 while the VPD-related partial correlation also became less negative in the semi-humid zone. In PF,
390 the SM-related partial correlation became more negative in the semi-humid and semi-arid zones,
391 whereas the VPD-related partial correlation became less negative in the semi-humid zone. Overall,
392 both SM and VPD constrained θ , but the constraints were generally stronger in PF, and their
393 temporal changes were regionally differentiated rather than spatially uniform.



394

395 **Figure 6. Spatial distribution and zonal means of partial correlations between forest LAI-TF**

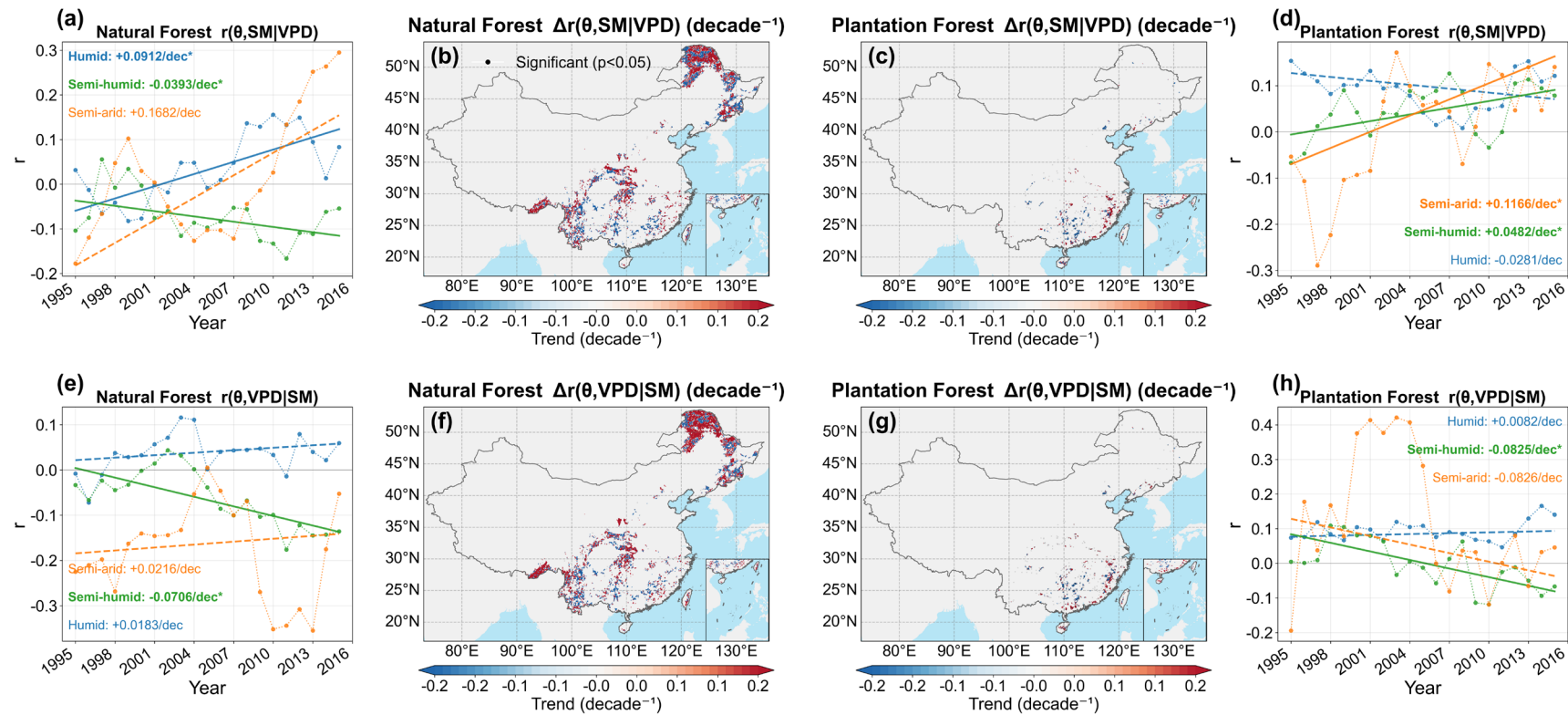
396 **sensitivity (θ) and hydroclimatic factors during the growing season from 1995 to 2015. (a) and**

397 **(b) show the spatial patterns of $r(\theta, SM|VPD)$ for natural forests (NF) and plantation forests (PF),**

398 **respectively; (c) and (d) show the corresponding patterns of $r(\theta, VPD|SM)$. (e) and (f) show the**

399 **mean partial correlations across climatic zones. All variables were Z-score standardized before**

400 **analysis, and pixels with fewer than 10 years of valid data were excluded.**



401

402

Figure 7. Temporal evolution and spatial trends of partial correlations between forest LAI–TF sensitivity (θ) and hydroclimatic factors during the growing

403

season from 1995 to 2015. (a) and (d) show the temporal evolution of zone-averaged $r(\theta, SM|VPD)$ for NF and PF, respectively; (b) and (c) show the corresponding

404

spatial trends. (e) and (h) show the temporal evolution of zone-averaged $r(\theta, VPD|SM)$ for NF and PF, respectively; (f) and (g) show the corresponding spatial trends.

405

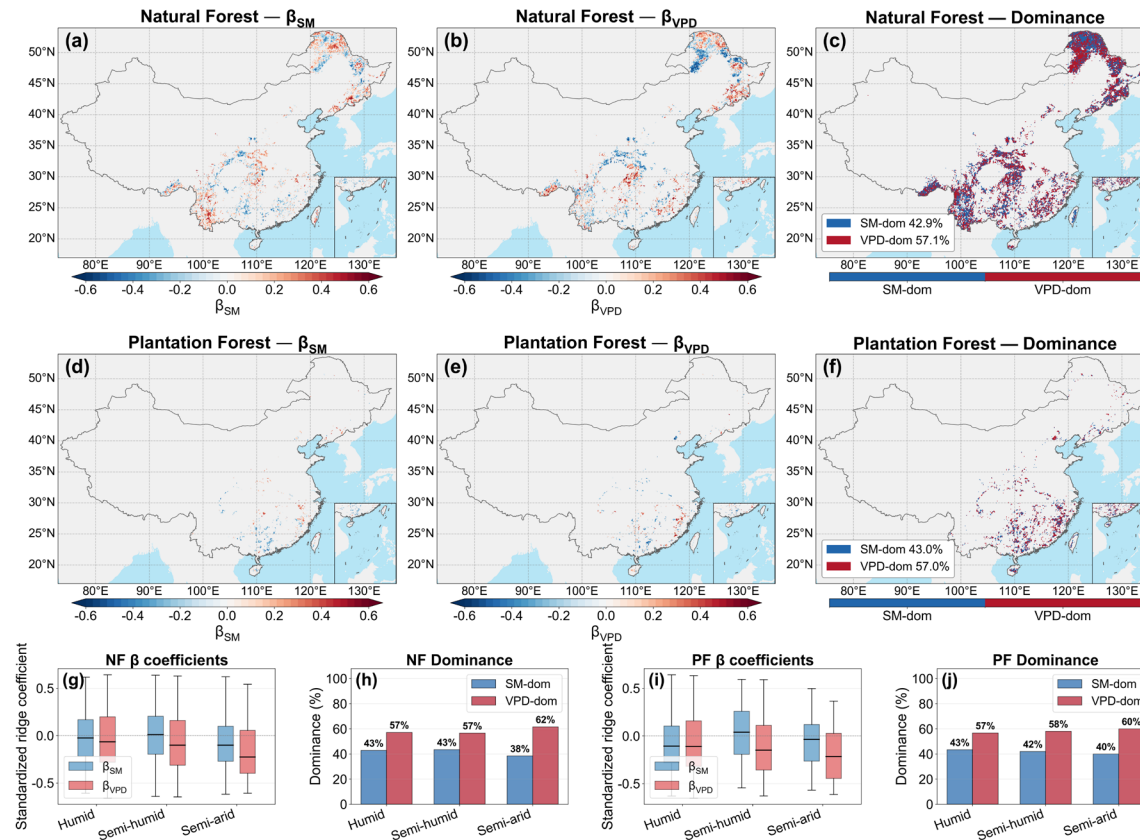
Trend slopes were estimated using the Theil–Sen estimator, and significant pixels according to the variance-corrected Mann–Kendall test ($p < 0.05$) are indicated by

406

black dots.

407 **3.2.3. Quantification and spatiotemporal heterogeneity of dominant**
408 **hydrological drivers**

409 Ridge regression showed that both SM and VPD were generally negatively associated with θ ,
410 but the magnitude was usually stronger for VPD (Figure 8). At the national scale, both NF and PF
411 remained slightly more VPD-dominated in terms of the present spatial pattern, with mean relative
412 contributions of VPD of 0.541 and 0.534 in NF and PF, respectively. Consistently, VPD-dominated
413 pixels accounted for 57.1% of all NF pixels and 57.0% of all PF pixels, compared with 42.9% and
414 43.0%, respectively, for SM-dominated pixels. The relative-contribution and dominance statistics
415 therefore consistently indicated a modest present-day advantage of VPD over SM, particularly in
416 the semi-arid zone. The trend analysis further indicated a general strengthening of the SM effect
417 and a weakening of the VPD effect in several regions, especially across semi-humid to semi-arid
418 areas (Figure 9). Within the pixel-wise temporal analysis, these results suggest that VPD explained
419 a slightly larger share of the spatial pattern of θ , whereas the relative role of SM increased over time.
420 RC and VIF supported the robustness of this interpretation (Figure S16).



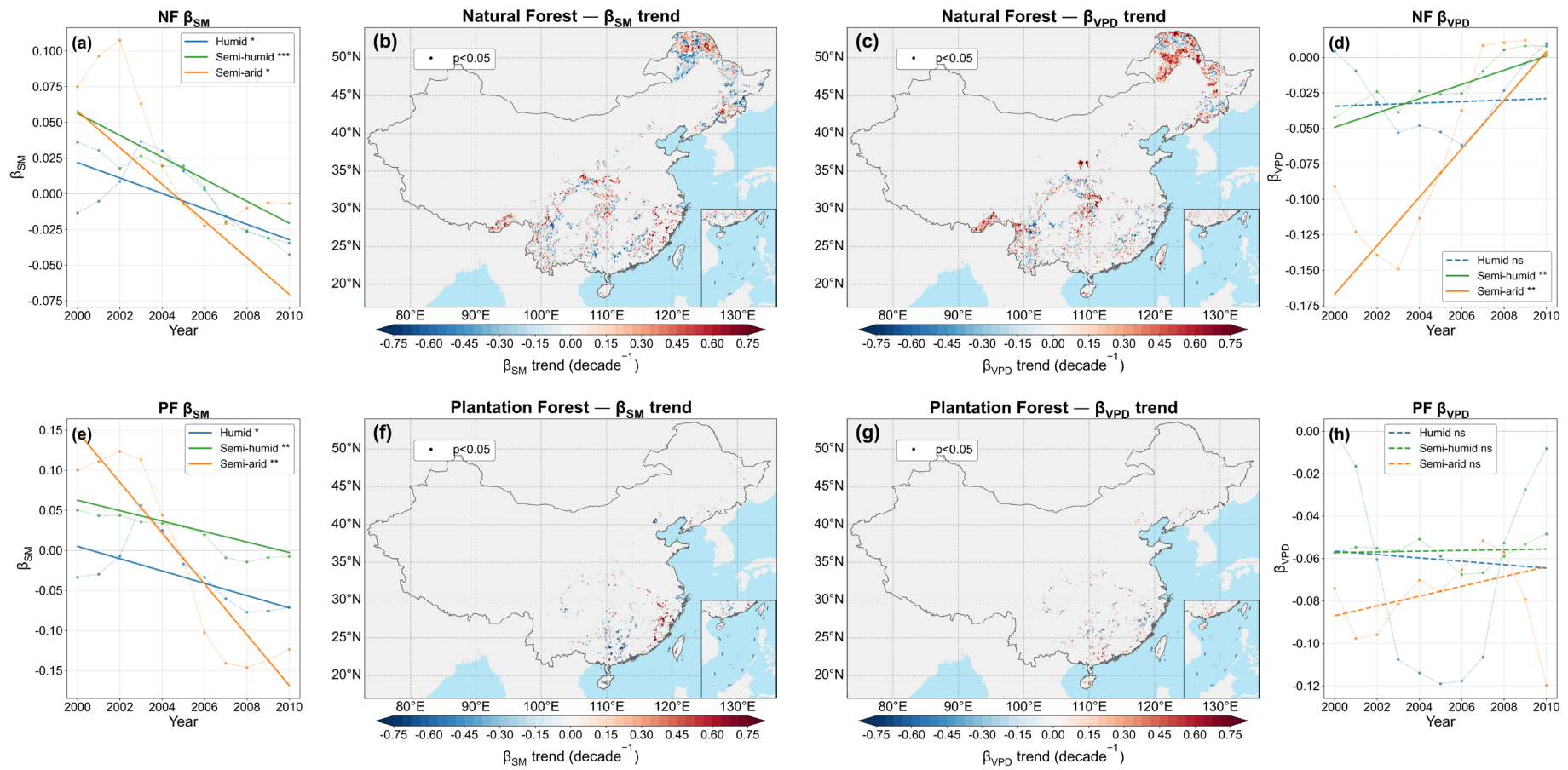
421

422 **Figure 8. Spatial distribution of ridge-regression standardized coefficients and dominant hydrological driver for forest θ .** For natural forests (NF), (a) and (b)

423 show the spatial distributions of β_{SM} and β_{VPD} , respectively, and (c) shows the corresponding dominance pattern. (d)–(f) show the same results for plantation forests

424 (PF). (g) and (i) show boxplots of pixel-level standardized β_{SM} and β_{VPD} across climatic zones for NF and PF, respectively. The central line denotes the median, boxes

425 indicate the interquartile range, whiskers extend to 1.5 times the interquartile range, and points outside the whiskers are shown as outliers. (h) and (j) show the fractions
 426 of SM- and VPD-dominated pixels across climatic zones. Warm colors indicate positive coefficients and cool colors indicate negative coefficients; blue and red in
 427 dominance maps denote SM-dominated and VPD-dominated pixels, respectively.

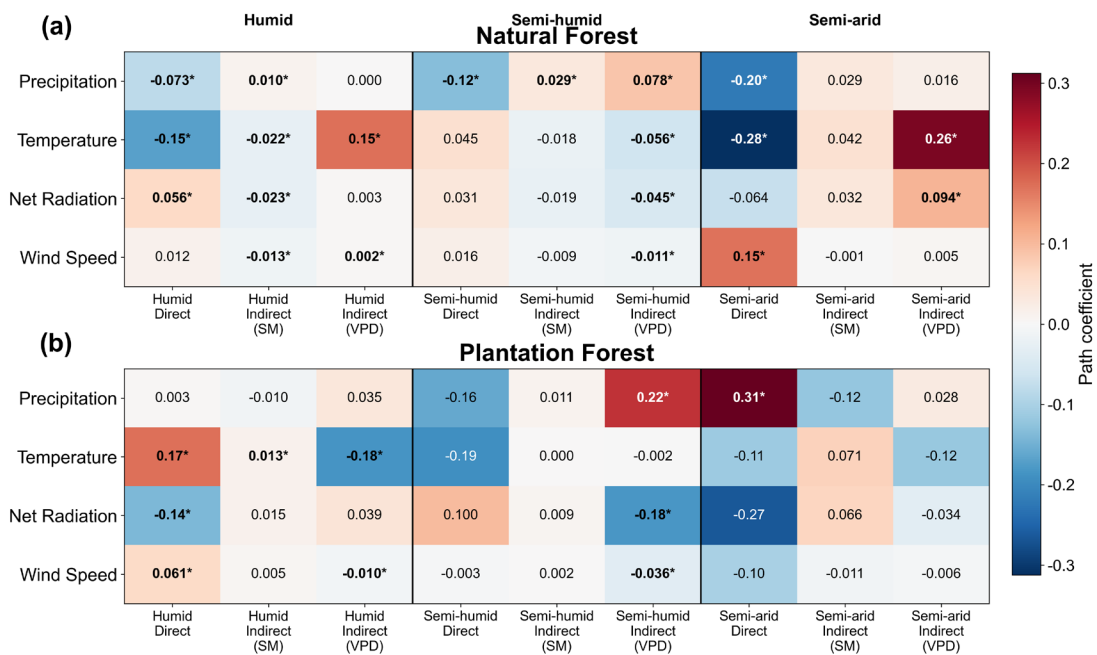


428

429 **Figure 9. Temporal evolution and spatial trends of ridge-regression coefficients for forest θ .** (a) and (e) show the temporal evolution of zone-averaged β_{SM} for NF
430 and PF, respectively; (b) and (f) show the corresponding spatial trends in β_{SM} . (d) and (h) show the temporal evolution of zone-averaged β_{VPD} for NF and PF, respectively;
431 (c) and (g) show the corresponding spatial trends in β_{VPD} . Trend slopes were estimated using the Theil–Sen estimator, and significant pixels based on the Mann–Kendall
432 test ($p < 0.05$) are indicated by black dots. Solid trend lines indicate significant trends, and dashed lines indicate non-significant trends.

433 **3.3. Pathway attribution of macro-climate effects on θ**

434 Pathway analysis indicated that the effects of macroclimate change on θ varied strongly among
 435 drivers, climatic zones, and forest types (Figure 10). In natural forests (NF), precipitation generally
 436 showed negative direct effects, especially in the semi-humid and semi-arid zones, while its indirect
 437 effects differed among pathways, including positive VPD-mediated effects in humid and semi-arid
 438 zones. Temperature was the most consistent negative direct driver in NF, with particularly strong
 439 negative effects in humid and semi-arid regions, while its indirect effects differed according to
 440 pathway, including positive VPD-mediated effects in humid and semi-arid zones. In plantation
 441 forests (PF), the pathway structure was more heterogeneous; specifically, precipitation showed a
 442 significant positive direct effect in the semi-arid zone, temperature showed opposite indirect effects
 443 through SM and VPD in the humid zone, and net radiation and wind speed mainly exerted pathway-
 444 specific effects in humid and semi-humid regions. Overall, the pathway coefficients indicated strong
 445 dependence on hydroclimatic context and forest type in how macroclimate trends were associated
 446 with changes in θ , with no single pathway dominating across all climate drivers and zones. A
 447 supplementary mediator-specification comparison showed that the direction of VPD-mediated
 448 indirect effects was generally more robust across single-mediator and joint models than that of SM-
 449 mediated effects, whereas SM-mediated pathways were more sensitive to model specification under
 450 SM–VPD coupling (Figure S19).



451

452 **Figure 10. Heatmap of pathway coefficients across climate zones for natural and plantation**
453 **forests.** Standardized path coefficients show the decomposition of the effects of four macroclimate
454 drivers (precipitation, temperature, net radiation, and wind speed) on θ_{total} trends into direct effects
455 and indirect effects mediated by SM and VPD for natural forests (a) and plantation forests (b). Rows
456 correspond to the four macro-climate drivers, while columns are grouped by climate zone (humid,
457 semi-humid, and semi-arid), each subdivided into direct effects, indirect effects via SM, and indirect
458 effects via VPD. Cell values are standardized coefficients from parallel dual-mediation pathway
459 analysis, and asterisks indicate significance at the 95% level (i.e., bootstrap confidence interval
460 excludes zero). Warm colors indicate positive effects, while cool colors indicate negative effects.

461 **4. Discussion**

462 **4.1. Nonlinear hydroclimatic regulation of θ**

463 The joint SM–VPD analysis shows that θ was highest under intermediate SM and moderate-
464 to-high VPD, corresponding to relatively strong atmospheric demand, and declined toward both
465 wetter/low-demand and drier/high-demand conditions (Figure 5; Figures S14–S15). This pattern
466 indicates that increased leaf area enhances TF most effectively when water supply is sufficient but
467 not excessive and evaporative demand is strong enough to sustain canopy transpiration. Once soil
468 water becomes limiting or atmospheric demand becomes too strong, stomatal regulation
469 increasingly constrains transpiration to avoid hydraulic damage, so the marginal gain in
470 transpiration per unit increase in LAI declines (Novick et al., 2016; Grossiord et al., 2020;
471 McDowell et al., 2022). Under wetter and weak-demand conditions, the capacity of additional leaf
472 area to increase TF is also reduced because energy limitations, weaker canopy–atmosphere coupling,
473 and larger non-transpirational evaporation fractions all weaken the translation of additional leaf area
474 into transpiration (Konings et al., 2017; Stoy et al., 2019). The θ decomposition and supplementary
475 diagnostics further suggest that this nonlinearity cannot be explained solely as a bounded geometric
476 effect of TF; part of the long-term change also reflects shifts in the LAI–TF relationship itself
477 (Figure 4; Figures S6–S13).

478 **4.2. Long-term weakening of the LAI enhancement effect on TF**

479 The widespread decline in θ , especially across semi-humid to semi-arid transition zones,
480 indicates that the capacity of increasing LAI to enhance TF has weakened over the last three decades

481 (Figure 3). This trend is consistent with a background of warming, rising VPD, and increasing
482 frequency of soil moisture limitation, all of which reduce the effective transpiration response of
483 forests to additional canopy development (Yuan et al., 2019; Lian et al., 2020; Denissen et al., 2022).
484 Rising atmospheric CO₂ may also have contributed to this decline by lowering stomatal conductance
485 and increasing intrinsic water-use efficiency, thereby reducing transpiration demand per unit leaf
486 area even where greening continued (Keenan et al., 2013; Keenan et al., 2016; Lavergne et al., 2019;
487 Liang et al., 2023). At the same time, the supplementary analyses are more consistent with
488 interpreting CO₂ as a temporally coherent background forcing rather than a spatially heterogeneous
489 driver of θ across China's forests (Figure S17; Table S1). Stand development may likewise have
490 modulated this trajectory. Age-related changes in stand structure, rooting depth, canopy roughness,
491 and interception can shift the partitioning of evapotranspiration between transpiration and non-
492 transpirational components, and therefore alter the LAI–TF relationship even without large changes
493 in total leaf area (Fan et al., 2017; Forrester, 2015). However, the age-stratified results show that the
494 higher θ in NF than in PF persisted across age groups, and including stand age did not overturn the
495 broad interpretation of the relative roles of SM and VPD, although the magnitude of change was
496 heterogeneous across forest types and climatic zones (Figure S18; Table S2). Together, these results
497 suggest that CO₂ rise and stand development may act as background modifiers of θ , while the
498 dominant large-scale patterns remain primarily associated with hydroclimatic variability.

499 **4.3. Temporal changes in hydroclimatic effects on θ**

500 Partial correlation, ridge regression, and pathway analysis consistently indicate that the
501 hydroclimatic controls on θ have changed over time, with the relative role of SM strengthening and
502 that of VPD weakening in many regions (Figures 6–10). This does not mean that atmospheric
503 demand has ceased to matter; VPD still explains a slightly larger share of the present spatial pattern
504 of θ , as also supported by the dominance statistics and multicollinearity diagnostics (Figure 8;
505 Figure S16). The more important point is that the sensitivity of θ to soil moisture limitation has
506 intensified under recent climatic conditions. This interpretation is physically consistent with the
507 increasing prevalence of water-limited ecosystem behavior under warming, in which rising
508 evaporative demand is increasingly translated into ecological stress through soil-water depletion
509 rather than through atmospheric forcing alone (Berg et al., 2016; Denissen et al., 2022). Once

510 ecosystems approach critical soil-moisture thresholds more frequently, stomatal and hydraulic
511 regulation become more tightly constrained by water supply, and the explanatory role of SM rises
512 accordingly (Fu et al., 2022; Liu et al., 2025). The pathway results add the same message at a broader
513 scale: temperature exerted generally negative effects on θ , whereas the effects of precipitation and
514 radiation varied by forest type and climatic zone, implying that macroclimate trends influence θ
515 through multiple hydroclimatic pathways rather than through a single dominant mechanism.

516 **4.4. Contrasting ecohydrological responses of natural and plantation forests**

517 The contrast between natural and plantation forests remained one of the clearest features of the
518 analysis. NF consistently showed higher θ , and high- θ values in NF were maintained across a wider
519 range of SM–VPD backgrounds, whereas PF showed lower θ and a more restricted range of
520 hydroclimatic conditions under which high θ occurred. This pattern likely reflects differences
521 between long-term spatial hydroclimatic contrasts and within-pixel temporal variability. Spatial
522 contrasts integrate longer-term differences in stand structure, species composition, hydraulic
523 diversity, and belowground water access, whereas temporal anomalies are expressed more directly
524 through canopy–atmosphere coupling and stomatal–hydraulic regulation during drought (Martínez-
525 Vilalta & García-Forner, 2017; Grossiord et al., 2020; Novick et al., 2024; Bachofen et al., 2024).
526 Under this interpretation, the broader hydroclimatic response of NF may reflect the greater structural
527 and functional heterogeneity often associated with natural forests, while the narrower response of
528 PF may reflect the relative structural simplification typical of many plantation stands. This
529 interpretation is also consistent with evidence that higher hydraulic diversity can buffer ecosystem
530 drought responses (Anderegg et al., 2018). The age-stratified supplementary results are consistent
531 with this interpretation, because the higher θ in NF than in PF persisted across age classes and this
532 pattern is therefore unlikely to be explained solely by stand age.

533 **4.5. Implications and limitations**

534 These results imply that further greening will not necessarily translate into proportionally
535 higher transpiration fractions under continued warming and drying. In regions where hydroclimatic
536 water stress is increasing, especially across semi-humid to semi-arid transition zones, the
537 ecohydrological consequences of increasing canopy leaf area depend increasingly on soil water

538 supply, and this dependence appears more evident in plantation forests than in natural forests. This
539 has direct management implications: plantation design may benefit from greater rooting-depth and
540 trait diversity and from stand structures that reduce rapid soil-water depletion, whereas natural
541 forests may benefit more from maintaining multilayer canopy structure and hydraulic diversity
542 under rising atmospheric demand. Several limitations should remain explicit. A nationwide in situ
543 benchmark for θ trends is not yet available because long-term observations that simultaneously
544 resolve transpiration partitioning, LAI dynamics, and stand development remain too sparse across
545 China's forests. We therefore evaluated robustness through cross-product consistency rather than
546 direct site-based validation. In addition, because θ , SM, and VPD were analyzed from growing-
547 season aggregates and moving-window series, the results characterize seasonal-to-interannual
548 hydroclimatic controls rather than instantaneous stomatal responses to short-lived atmospheric
549 fluctuations. Even with these constraints, the convergence among the main analyses, the
550 supplementary robustness checks, and the CO₂- and age-sensitivity diagnostics supports the central
551 inference that the enhancement of TF by increasing LAI has weakened across China's forests and
552 is increasingly shaped by soil moisture limitation.

553 **5. Conclusion**

554 Across China's forests, the enhancement of TF caused by increased LAI has weakened during
555 1990–2020. VPD still explains a slightly larger share of the present spatial pattern of θ , but the role
556 of SM has strengthened over this timespan, indicating there has been an increase in SM limitation.
557 Differences between NF and PF were obvious: NF maintained higher θ values, whereas PF showed
558 a greater long-term decline in θ . Collectively, these results indicate that continued greening under
559 warming will not necessarily result in proportionally higher TF, particularly in semi-humid to semi-
560 arid transition regions.

561 **Author contributions**

562 Xiao Zhang performed the analysis, prepared the figures, and drafted the manuscript. Xinxiao
563 Yu contributed to the study design, interpretation of the results, and manuscript revision. Guodong
564 Jia conceived and supervised the study, contributed to the analytical framework, and revised the
565 manuscript. All authors discussed the results and approved the final manuscript.

566 **Competing interests**

567 The authors declare that they have no conflict of interest.

568 **Code and data availability**

569 The datasets used in this study are publicly available from the sources cited in Table 1. The
570 processed data and code supporting the findings of this study are available from the corresponding
571 author upon reasonable request.

572 **Funding**

573 This research was supported by the National Key Research and Development Program of China
574 (No. 2023YFF1305302) and the National Natural Science Foundation of China (Nos. 42277062,
575 42230714).
576

577 **References**

- 578 Anderegg, W.R.L., Konings, A.G., Trugman, A.T., Yu, K., Bowling, D.R., Gabbitas, R., Karp,
579 D.S., Pacala, S., Sperry, J.S., Sulman, B.N. and Zenes, N. (2018) Hydraulic diversity of forests
580 regulates ecosystem resilience during drought. *Nature*, 561, 538–541. doi:10.1038/s41586-018-
581 0539-7
- 582 Bachofen, C., Tumber-Dávila, S.J., Mackay, D.S., McDowell, N.G., Carminati, A., Klein, T.,
583 Stocker, B.D., Mencuccini, M. and Grossiord, C. (2024) Tree water uptake patterns across the globe.
584 *New Phytologist*, 242, 1891–1910. doi:10.1111/nph.19762
- 585 Berg, A., Findell, K., Lintner, B., Giannini, A., Seneviratne, S.I., van den Hurk, B., Lorenz, R.,
586 Pitman, A.J., Hagemann, S., Meier, A., Cheruy, F., Ducharne, A., Malyshev, S. and Milly, P.C.D.
587 (2016) Land–atmosphere feedbacks amplify aridity increase over land under global warming.
588 *Nature Climate Change*, 6, 869–874. doi:10.1038/nclimate3029
- 589 Buck, A.L. (1981) New equations for computing vapor pressure and enhancement factor.
590 *Journal of Applied Meteorology*, 20, 1527–1532. doi:10.1175/1520-
591 0450(1981)020<1527:NEFCVP>2.0.CO;2
- 592 Cao, S., Li, M., Zhu, Z., Wang, Z., Zha, J., Zhao, W., Duanmu, Z., Chen, J., Zheng, Y., Chen,
593 Y., Myneni, R.B. and Piao, S. (2023) Spatiotemporally consistent global dataset of the GIMMS leaf
594 area index (GIMMS LAI4g) from 1982 to 2020. *Earth System Science Data*, 15, 4877–4899.
595 doi:10.5194/essd-15-4877-2023
- 596 Chen, H., Wei, Y. and Huang, J.J. (2024) Widespread increase in plant transpiration driven by
597 global greening. *Global and Planetary Change*, 235, 104395. doi:10.1016/j.gloplacha.2024.104395
- 598 Cheng, K., Chen, Y., Xiang, T., Yang, H., Liu, W., Ren, Y., Guan, H., Hu, T., Ma, Q. and Guo,
599 Q. (2024a) A 2020 forest age map for China with 30 m resolution. *Earth System Science Data*, 16,
600 803–819. doi:10.5194/essd-16-803-2024
- 601 Cheng, K., Yang, H., Guan, H., Ren, Y., Chen, Y., Chen, M., Yang, Z., Lin, D., Liu, W., Xu,
602 J., Xu, G., Ma, K. and Guo, Q. (2024b) Unveiling China’s natural and planted forest spatial–
603 temporal dynamics from 1990 to 2020. *ISPRS Journal of Photogrammetry and Remote Sensing*,
604 209, 37–50. doi:10.1016/j.isprsjprs.2024.01.024
- 605 Cheng, K., Zhang, Y., Yang, H., Ren, Y., Xiang, T., Chen, Y., Yang, Z., Chen, M., Xu, J.,
606 Huang, G., Xu, G., Tao, S., Yu, Z. and Guo, Q. (2025) China’s naturally regenerated forests
607 currently have greater aboveground carbon accumulation rates than newly planted forests.
608 *Communications Earth & Environment*, 6, 345. doi:10.1038/s43247-025-02323-z
- 609 Denissen, J.M.C., Teuling, A.J., Pitman, A.J., Koirala, S., Migliavacca, M., Li, W., Reichstein,
610 M., Winkler, A.J., Zhan, C. and Orth, R. (2022) Widespread shift from ecosystem energy to water
611 limitation with climate change. *Nature Climate Change*, 12, 677–684. doi:10.1038/s41558-022-
612 01403-8
- 613 Fan, Y., Miguez-Macho, G., Jobbágy, E.G., Jackson, R.B. and Otero-Casal, C. (2017)
614 Hydrologic regulation of plant rooting depth. *Proceedings of the National Academy of Sciences of*
615 *the United States of America*, 114, 10572–10577. doi:10.1073/pnas.1712381114
- 616 Farooq, T.H., Shakoor, A., Wu, X., Li, Y., Rashid, M.H.U., Zhang, X., Gilani, M.M., Kumar,
617 U., Chen, X. and Yan, W. (2021) Perspectives of plantation forests in the sustainable forest

618 development of China. *iForest - Biogeosciences and Forestry*, 14, 166–174. doi:10.3832/ifor3551-
619 014

620 Forrester, D.I. (2015) Transpiration and water-use efficiency in mixed-species forests versus
621 monocultures: effects of tree size, stand density and season. *Tree Physiology*, 35, 289–304.
622 doi:10.1093/treephys/tpv011

623 Fu, Z., Ciais, P., Feldman, A., Gentine, P., Makowski, D., Prentice, I.C., Stoy, P.C., Bastos, A.
624 and Wigneron, J.-P. (2022) Critical soil moisture thresholds of plant water stress in terrestrial
625 ecosystems. *Science Advances*, 8, eabq7827. doi:10.1126/sciadv.abq7827

626 Grossiord, C., Buckley, T.N., Cernusak, L.A., Novick, K.A., Poulter, B., Siegwolf, R.T.W.,
627 Sperry, J.S. and McDowell, N.G. (2020) Plant responses to rising vapor pressure deficit. *New
628 Phytologist*, 226, 1550–1566. doi:10.1111/nph.16485

629 Hu, Y., Wei, F., Fu, B. and Zhang, W. (2023) Ecosystems in China have become more sensitive
630 to changes in water demand since 2001. *Communications Earth & Environment*, 4, 444.
631 doi:10.1038/s43247-023-01105-9

632 Keenan, T.F., Hollinger, D.Y., Bohrer, G., Dragoni, D., Munger, J.W., Schmid, H.P. and
633 Richardson, A.D. (2013) Increase in forest water-use efficiency as atmospheric carbon dioxide
634 concentrations rise. *Nature*, 499, 324–327. doi:10.1038/nature12291

635 Keenan, T.F., Prentice, I.C., Canadell, J.G., Williams, C.A., Wang, H., Raupach, M. and
636 Collatz, G.J. (2016) Recent pause in the growth rate of atmospheric CO₂ due to enhanced terrestrial
637 carbon uptake. *Nature Communications*, 7, 13428. doi:10.1038/ncomms13428

638 Koehler, T., Wankmüller, F.J.P., Sadok, W. and Carminati, A. (2023) Transpiration response
639 to soil drying versus increasing vapor pressure deficit in crops: physical and physiological
640 mechanisms and key plant traits. *Journal of Experimental Botany*, 74, 4789–4807.
641 doi:10.1093/jxb/erad221

642 Konings, A.G., Williams, A.P. and Gentine, P. (2017) Sensitivity of grassland productivity to
643 aridity controlled by stomatal and xylem regulation. *Nature Geoscience*, 10, 284–288.
644 doi:10.1038/ngeo2903

645 Lavergne, A., Graven, H., De Kauwe, M.G., Keenan, T.F., Medlyn, B.E. and Prentice, I.C.
646 (2019) Observed and modelled historical trends in the water-use efficiency of plants and ecosystems.
647 *Global Change Biology*, 25, 2242–2257. doi:10.1111/gcb.14634

648 Li, C., Han, J., Liu, Z., Tu, Z. and Yang, H. (2024) A harmonized global gridded transpiration
649 product based on collocation analysis. *Scientific Data*, 11, 604. doi:10.1038/s41597-024-03425-7

650 Lian, X., Piao, S., Li, L.Z.X., Li, Y., Huntingford, C., Ciais, P., Cescatti, A., Janssens, I.A.,
651 Peñuelas, J., Buermann, W., Chen, A., Li, X., Myneni, R.B., Wang, X., Wang, Y., Yang, Y., Zeng,
652 Z., Zhang, Y. and McVicar, T.R. (2020) Summer soil drying exacerbated by earlier spring greening
653 of northern vegetation. *Science Advances*, 6, eaax0255. doi:10.1126/sciadv.aax0255

654 Liang, X., Wang, D., Ye, Q., Zhang, J., Liu, M., Liu, H., Yu, K., Wang, Y., Hou, E., Zhong,
655 B., Xu, L., Lv, T., Peng, S., Lu, H., Sicard, P., Anav, A. and Ellsworth, D.S. (2023) Stomatal

656 responses of terrestrial plants to global change. *Nature Communications*, 14, 2188.
657 doi:10.1038/s41467-023-37934-7

658 Liu, L., Gudmundsson, L., Hauser, M., Qin, D., Li, S. and Seneviratne, S.I. (2020a) Soil
659 moisture dominates dryness stress on ecosystem production globally. *Nature Communications*, 11,
660 4892. doi:10.1038/s41467-020-18631-1

661 Liu, Y., Kumar, M., Katul, G.G., Feng, X. and Konings, A.G. (2020b) Plant hydraulics
662 accentuates the effect of atmospheric moisture stress on transpiration. *Nature Climate Change*, 10,
663 691–695. doi:10.1038/s41558-020-0781-5

664 Liu, Y., Lin, Z., Wang, Z., Chen, X., Han, P., Wang, B., Wang, Z., Wen, Z., Shi, H., Zhang, Z.
665 and Zhang, W. (2023) Discriminating the impacts of vegetation greening and climate change on the
666 changes in evapotranspiration and transpiration fraction over the Yellow River Basin. *Science of
667 the Total Environment*, 904, 166926. doi:10.1016/j.scitotenv.2023.166926

668 Liu, Y., Wang, Y., Zhao, Y., Chen, S., Wang, L., Yang, W., Li, X., Li, X., Lei, H., Chang, H.,
669 Zhai, J., Zhu, Y., Wang, Q. and Ye, T. (2025) Evapotranspiration stress intensifies with enhanced
670 sensitivity to soil moisture deficits in a rapidly greening China. *Hydrology and Earth System
671 Sciences*, 29, 3379–3404. doi:10.5194/hess-29-3379-2025

672 Martínez-Vilalta, J. and García-Forner, N. (2017) Water potential regulation, stomatal
673 behaviour and hydraulic transport under drought: deconstructing the iso/anisohydric concept. *Plant,
674 Cell & Environment*, 40, 962–976. doi:10.1111/pce.12846

675 McDowell, N.G., Sapes, G., Pivovarov, A., Adams, H.D., Allen, C.D., Anderegg, W.R.L.,
676 Arend, M., Breshears, D.D., Brodrick, T., Choat, B., Cochard, H., De Cáceres, M., De Kauwe, M.G.,
677 Grossiord, C., Hammond, W.M., Hartmann, H., Hoch, G., Kahmen, A., Klein, T., Mackay, D.S.,
678 Mantova, M., Martínez-Vilalta, J., Medlyn, B.E., Mencuccini, M., Nardini, A., Oliveira, R.S., Sala,
679 A., Tissue, D.T., Torres-Ruiz, J.M., Trowbridge, A.M., Trugman, A.T., Wiley, E. and Xu, C. (2022)
680 Mechanisms of woody-plant mortality under rising drought, CO₂ and vapour pressure deficit. *Nature
681 Reviews Earth & Environment*, 3, 294–308. doi:10.1038/s43017-022-00272-1

682 Miralles, D.G., Bonte, O., Koppa, A., Baez-Villanueva, O.M., Tronquo, E., Zhong, F., Beck,
683 H.E., Hulsman, P., Dorigo, W., Verhoest, N.E.C. and Haghdoost, S. (2025) GLEAM4: global land
684 evaporation and soil moisture dataset at 0.1° resolution from 1980 to near present. *Scientific Data*,
685 12, 416. doi:10.1038/s41597-025-04610-y

686 Muñoz-Sabater, J., Dutra, E., Agustí-Panareda, A., Albergel, C., Arduini, G., Balsamo, G.,
687 Boussetta, S., Choulga, M., Harrigan, S., Hersbach, H., Martens, B., Miralles, D.G., Piles, M.,
688 Rodríguez-Fernández, N.J., Zsoter, E., Buontempo, C. and Thépaut, J.-N. (2021) ERA5-Land: a
689 state-of-the-art global reanalysis dataset for land applications. *Earth System Science Data*, 13, 4349–
690 4383. doi:10.5194/essd-13-4349-2021

691 Niu, Z., He, H., Zhu, G., Ren, X., Zhang, L. and Zhang, K. (2020) A spatial-temporal
692 continuous dataset of the transpiration to evapotranspiration ratio in China from 1981–2015.
693 *Scientific Data*, 7, 369. doi:10.1038/s41597-020-00693-x

694 Novick, K.A., Ficklin, D.L., Stoy, P.C., Williams, C.A., Bohrer, G., Oishi, A.C., Papuga, S.A.,
695 Blanken, P.D., Noormets, A., Sulman, B.N., Scott, R.L., Wang, L. and Phillips, R.P. (2016) The

696 increasing importance of atmospheric demand for ecosystem water and carbon fluxes. *Nature*
697 *Climate Change*, 6, 1023–1027. doi:10.1038/nclimate3114

698 Novick, K.A., Ficklin, D.L., Grossiord, C., Konings, A.G., Martínez-Vilalta, J., Sadok, W.,
699 Trugman, A.T., Williams, A.P., Wright, A.J., Abatzoglou, J.T., Dannenberg, M.P., Gentine, P.,
700 Guan, K., Johnston, M.R., Lowman, L.E.L., Moore, D.J.P. and McDowell, N.G. (2024) The impacts
701 of rising vapour pressure deficit in natural and managed ecosystems. *Plant, Cell & Environment*, 47,
702 3561–3589. doi:10.1111/pce.14846

703 Qing, Y., Wang, S., Ancell, B.C. and Yang, Z.-L. (2022) Accelerating flash droughts induced
704 by the joint influence of soil moisture depletion and atmospheric aridity. *Nature Communications*,
705 13, 1139. doi:10.1038/s41467-022-28752-4

706 Schlesinger, W.H. and Jasechko, S. (2014) Transpiration in the global water cycle. *Agricultural*
707 *and Forest Meteorology*, 189–190, 115–117. doi:10.1016/j.agrformet.2014.01.011

708 Song, J., Zhou, S., Yu, B., Li, Y., Liu, Y., Yao, Y., Wang, S. and Fu, B. (2024) Serious
709 underestimation of reduced carbon uptake due to vegetation compound droughts. *npj Climate and*
710 *Atmospheric Science*, 7, 23. doi:10.1038/s41612-024-00571-y

711 Stoy, P.C., El-Madany, T.S., Fisher, J.B., Gentine, P., Gerken, T., Good, S.P., Klosterhalfen,
712 A., Liu, S., Miralles, D.G., Perez-Priego, O., Rigden, A.J., Skaggs, T.H., Wohlfahrt, G., Anderson,
713 R.G., Coenders-Gerrits, A.M.J., Jung, M., Maes, W.H., Mammarella, I., Mauder, M., Migliavacca,
714 M., Nelson, J.A., Poyatos, R., Reichstein, M., Scott, R.L. and Wolf, S. (2019) Reviews and
715 syntheses: turning the challenges of partitioning ecosystem evaporation and transpiration into
716 opportunities. *Biogeosciences*, 16, 3747–3775. doi:10.5194/bg-16-3747-2019

717 Sun, S., Liu, Y., Chen, H., Ju, W., Xu, C.-Y., Liu, Y., Zhou, B., Zhou, Y., Zhou, Y. and Yu,
718 M. (2022) Causes for the increases in both evapotranspiration and water yield over vegetated
719 mainland China during the last two decades. *Agricultural and Forest Meteorology*, 324, 109118.
720 doi:10.1016/j.agrformet.2022.109118

721 Wang, J. (2026) Global daily 1 km gapless XCO₂ (2003–2023) derived from multi-satellite
722 observations and a spatiotemporal deep learning framework. *Environmental Impact Assessment*
723 *Review*, 117, 108146. doi:10.1016/j.eiar.2025.108146

724 Wei, Z., Yoshimura, K., Wang, L., Miralles, D.G., Jasechko, S. and Lee, X. (2017) Revisiting
725 the contribution of transpiration to global terrestrial evapotranspiration. *Geophysical Research*
726 *Letters*, 44, 2792–2801. doi:10.1002/2016GL072235

727 Xia, J., Xia, X., Chen, Y., Shen, R., Zhang, Z., Liang, B., Wang, J. and Yuan, W. (2023)
728 Reconstructing long-term forest age of China by combining forest inventories, satellite-based forest
729 age and forest cover data sets. *Journal of Geophysical Research: Biogeosciences*, 128,
730 e2023JG007492. doi:10.1029/2023JG007492

731 Xu, H., Yue, C., Zhang, Y., Liu, D. and Piao, S. (2023) Forestation at the right time with the
732 right species can generate persistent carbon benefits in China. *Proceedings of the National Academy*
733 *of Sciences of the United States of America*, 120, e2304988120. doi:10.1073/pnas.2304988120

734 Yuan, W., Zheng, Y., Piao, S., Ciais, P., Lombardozzi, D., Wang, Y., Ryu, Y., Chen, G., Dong,
735 W., Hu, Z., Jain, A.K., Jiang, C., Kato, E., Li, S., Lienert, S., Liu, S., Nabel, J.E.M.S., Qin, Z., Quine,
736 T., Sitch, S., Smith, W.K., Wang, F., Wu, C., Xiao, Z. and Yang, S. (2019) Increased atmospheric

737 vapor pressure deficit reduces global vegetation growth. *Science Advances*, 5, eaax1396.
738 doi:10.1126/sciadv.aax1396

739 Zahra, N., Hafeez, M.B., Kausar, A., Al Zeidi, M., Asekova, S., Siddique, K.H.M. and Farooq,
740 M. (2023) Plant photosynthetic responses under drought stress: effects and management. *Journal of*
741 *Agronomy and Crop Science*, 209, 651–672. doi:10.1111/jac.12652

742 Zhang, K., Chen, H., Ma, N., Shang, S., Wang, Y., Xu, Q. and Zhu, G. (2024) A global dataset
743 of terrestrial evapotranspiration and soil moisture dynamics from 1982 to 2020. *Scientific Data*, 11,
744 445. doi:10.1038/s41597-024-03271-7

745 Zhou, S., Zhang, Y., Williams, A.P. and Gentine, P. (2019) Projected increases in intensity,
746 frequency, and terrestrial carbon costs of compound drought and aridity events. *Science Advances*,
747 5, eaau5740. doi:10.1126/sciadv.aau5740

748